SCIENTIFIC REPORTS

OPEN

SUBJECT AREAS:
PHOTOCATALYSIS
CHEMICAL PHYSICS

Received
23 September 2013

Accepted
20 January 2014

Published
5 February 2014

Correspondence and requests for materials should be addressed to Y.D. (daiy60@sina.com)

Noble-metal-free plasmonic photocatalyst: hydrogen doped semiconductors

Xiangchao Ma[1], Ying Dai[1], Lin Yu[1] & Baibiao Huang[2]

[1]School of Physics, State Key Laboratory of Crystal Materials, Shandong University, Jinan 250100, People's Republic of China, [2]State Key Laboratory of Crystal Materials, Shandong University, Jinan 250100, People's Republic of China.

The unique capacity of localized surface plasmon resonance (LSPR) offers a new opportunity to overcome the limited efficiency of semiconductor photocatalyst. Here we unravel that LSPR, which usually occurs in noble metal nanoparticles, can be realized by hydrogen doping in noble-metal-free semiconductor using TiO_2 as a model photocatalyst. Moreover, its LSPR is located in infrared region, which supplements that of noble metal whose LSPR is generally in the visible region, making it possible to extend the light response of photocatalyst to infrared region. The near field enhancement is shown to be comparable with that of noble-metal nanoparticles, indicating that highly enhanced light absorption rate can be expected. The present work can provide a key guideline for the creation of highly efficient noble-metal-free plasmonic photocatalysts and have a much wider impact in infrared bioimaging and spectroscopy where infrared LSPR is essential.

Despite four decades of efforts including doping[1–3], heterojunction[4,5], graphene-based composition[6,7], and cocatalyst[8,9] to improve their photocatalytic performance, large-scale application of photocatalysts, such as TiO_2 and ZnO, is still significantly inhibited by their narrow light absorption range and large carrier recombination rate[10–12]. More recently, the localized surface plasmon resonance (LSPR) of noble metal nanoparticles (NPs) is introduced into the field of photocatalysis[13,14], and the unique capacity of LSPR to amplify electromagnetic field and scatter electromagnetic radiation for a wide range of solar light wavelengths offers a new opportunity to overcome the limited efficiency of semiconductor photocatalyst. For example, depositing Ag or Au nanoparticles on TiO_2 significantly enhance the photocatalytic quantum efficiency and extend the light absorption range[15–17]. Our group also synthesized the classic Ag@AgX (X = Cl, Br, I) plasmonic photocatalysts[18–21] which show remarkable absorption over the whole ultraviolet and visible light range. However, it is noteworthy that the degradation of noble metals especially silver on exposure to air will significantly reduce the lifetime of this kind of plasmonic photocatalyst[22], the high cost and heavy metal pollution will also limit their large-scale application. In addition, the large carrier concentration and interband transition often lead to prominent energy loss. On the other hand, studies aimed at utilizing near-infrared light constituting about 44% of sunlight are relatively rare[23,24]. Therefore, exploring a noble-metal-free photocatalyst with LSPR effect in the near-infrared range has great scientific value and practical meaning.

As is known, the LSPR may occur as the free carrier concentration in NPs is large enough, thus we aim to explore the possibility of realizing LSPR in the commonly used semiconductor photocatalyst TiO_2 by heavy doping. Since TiO_2 samples are never perfectly stoichiometric, and are usually in reduced form showing n-type conductivity[25], we pay our attention on the n-type doping. To achieve heavy doping, there are two particular requirements of the dopant: solid solubility and donor level. Recently, it is experimentally reported that the electron carrier concentration of TiO_2 could reach $7.8 \times 10^{20}/cm^3$ after hydrogen plasma treatment[25], indicating that hydrogen may have a good solubility and moderate donor level, and they tentatively attribute the strong visible and infrared light absorption to the LSPR induced by this high carrier concentration. By the way, it is one of our purposes to verify the origin of the large carrier concentration and if the concentration could induce LSPR and hence contribute to the light absorption. In addition, it has been proved that the activation energy for atomic H diffusion into the TiO_2 crystal lattice is only about 0.09 eV[26], then hydrogen can be easily introduced into the crystal lattice. Considering the experimental results above, it seems that hydrogen is one of the idealistic dopants for realizing high carrier concentration in TiO_2. As our previous work has shown that hydrogen adsorption on the surface atoms of TiO_2 does not introduce free carriers[27] and a recent work demonstrated that the conduction band

minimum (CBM) electrons in anatase are neither very sensitive to local lattice distortions nor to changes induced by bonding to H[28], our attention here is mainly paid to hydrogen bulk doping. Therefore, in the present work, the solubility and donor level of H_i (hydrogen interstitial) and H_O (substituting host oxygen with hydrogen) is systematically studied to estimate the carrier concentration that can be achieved by hydrogen doping. Furthermore, on the basis of the Drude model[29,30] the critical carrier concentration for achieving LSPR at wavelengths relevant to photocatalysis is estimated. The LSPR absorption spectra and enhanced electric field distribution are also investigated based on the discrete dipole approximation (DDA)[31,32]. The results indicate that the necessary carrier concentration to realize LSPR in semiconductor can actually be achieved by hydrogen doping, and the LSPR can extend the light absorption to infrared wavelengths as well as significantly enhance the local electric field. To the best of our knowledge, we are the first to theoretically demonstrate the LSPR effect in the near-infrared range that can actually be realized by heavy hydrogen doping in TiO_2, and at the moment there is no experimental report about the LSPR in hydrogen doped TiO_2 to which we expect relevant experimental efforts to be devoted.

Results

Solubility and donor level. In thermodynamic equilibrium, the solubility of dopant in the semiconductor lattice is determined by the formation energy E_f through equation (1)

$$c = N_{sites} \exp(-E_f/kT) \quad (1)$$

Where c is the resultant concentration of dopant, N_{sites} is the number of sites in the lattice where the dopant can be incorporated, k is Boltzmann's constant, and T is temperature in kelvin. The formation energies of H_i and H_O in charge state q are defined as[33]

$$E_f(H_i^q) = E(H_i^q) - E(host) - E(H) + qE_F \quad (2)$$

$$E_f(H_O^q) = E(H_O^q) - E(host) - E(H) + \frac{1}{2}E(O_2) + qE_F \quad (3)$$

Where $E(\alpha)$is the total energy of system α. The reference for hydrogen energy is given by an H atom assuming hydrogen plasma environment and that for oxygen energy is given by an O_2 molecule since the substituted oxygen atoms generally form O_2 molecules. The last term in the formation energy accounts for the fact that H_i^+ (H_O^+) donates an electron, and H_i^- (H_O^-) accepts an electron; E_F denotes the energy of the reservoir with which these electrons are exchanged and is equal to the Fermi level of the system. By the way, we note that if one use H_2 molecule as dopant source, the formation energy will be increased by 2.27 eV due to the large binding energy of hydrogen in H_2. As a result, the solubility will be significantly reduced.

For H_i, a variety of possible interstitial sites are investigated to identify the stable location of H_i in TiO_2, and two local stable sites are determined with an energy difference of 0.53 eV between them, which is consistent with a previous report[34]. In the following we mainly focus on the most stable configuration (Figure 1b), since it is the dominant species from the perspective of thermodynamic stability. Figure 2 shows the formation energies of H_i and H_O in different charge states with respect to the Fermi level. The formation energy of neutral H_i is negative with a value of −1.88 eV, which indicates a release of energy upon the defect formation; and that of positive H_i is even more negative across the bandgap. Hence we infer that this kind of doping is highly favored according to equation (1), and one may expect an almost indefinite increase in the doping concentration once the hydrogen atom crosses the crystal surface and diffuses into the lattice. Fortunately, it is revealed that the energy barrier for the H atoms to migrate from the crystal surface into the bulk is quite moderate with a value of 0.70 eV[35] and the transfer barrier of H atom in the lattice is experimentally determined to be only about 0.09 eV[26]. Therefore, the incorporation of hydrogen into TiO_2 lattice to a high solid solubility is experimentally achievable. However, it has to be kept in mind that the defect formation energy is also a function of its concentration, and it increases with increasing concentration. Thus the doping concentration will not increase infinitely. Nevertheless, the formation energy of H_i corresponding to a concentration of about $7.41 \times 10^{21}/cm^3$ is only increased to −1.33 eV, then doping concentration in this order of magnitude or higher can be realized in H_i doped TiO_2. In addition, it is indicated that H_2 readily dissociates and forms two HO species exothermically[36], thus the high concentration of H_i will not form H_2 which eliminates the donor properties of H_i.

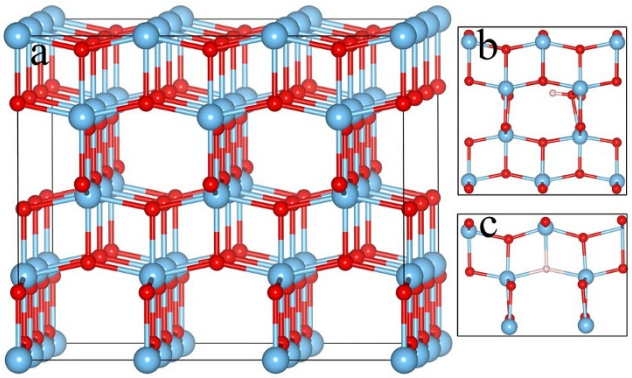

Figure 1 | The crystal structures used for our calculations. (a) The supercell model. The local geometric structures of (b) H_i and (c) H_O doped TiO_2. The sky blue, red, and pink balls represent Ti, O, and H atoms, respectively.

For the case of neutral H_O defect, the formation energy with a value of 1.84 eV is obtained. At equilibrium, the H_O concentration is estimated to be on the order of magnitude of $10^{11}/cm^3$ by hydrogen plasma treatment at 500°C. And the smaller formation energy of positive H_O across the bandgap implies a larger solubility. Moreover, once the oxygen vacancy (O_V) previously forms during the preparation process of TiO_2, which is the usual case, the formation energy will reduce to −3.13 eV. This large negative value clearly indicates readily occupation of H atoms in the oxygen vacancy sites, thus fully eliminating the oxygen vacancies in the host lattice, and its beneficial results will be discussed in the following.

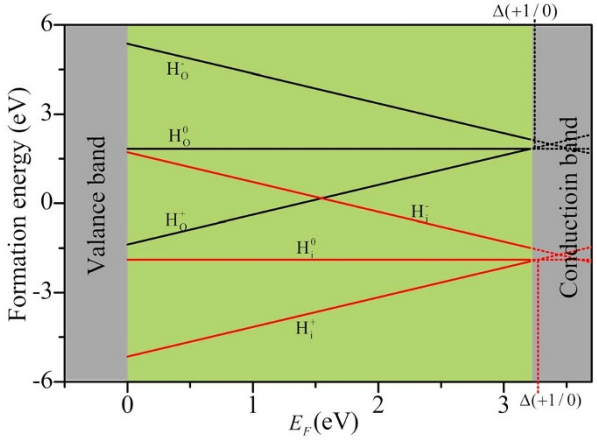

Figure 2 | Formation energies of H_i and H_O in different charge states with respect to the Fermi level E_F. The range of E_F corresponds to the bandgap with $E_F = 0$ at the VBM.

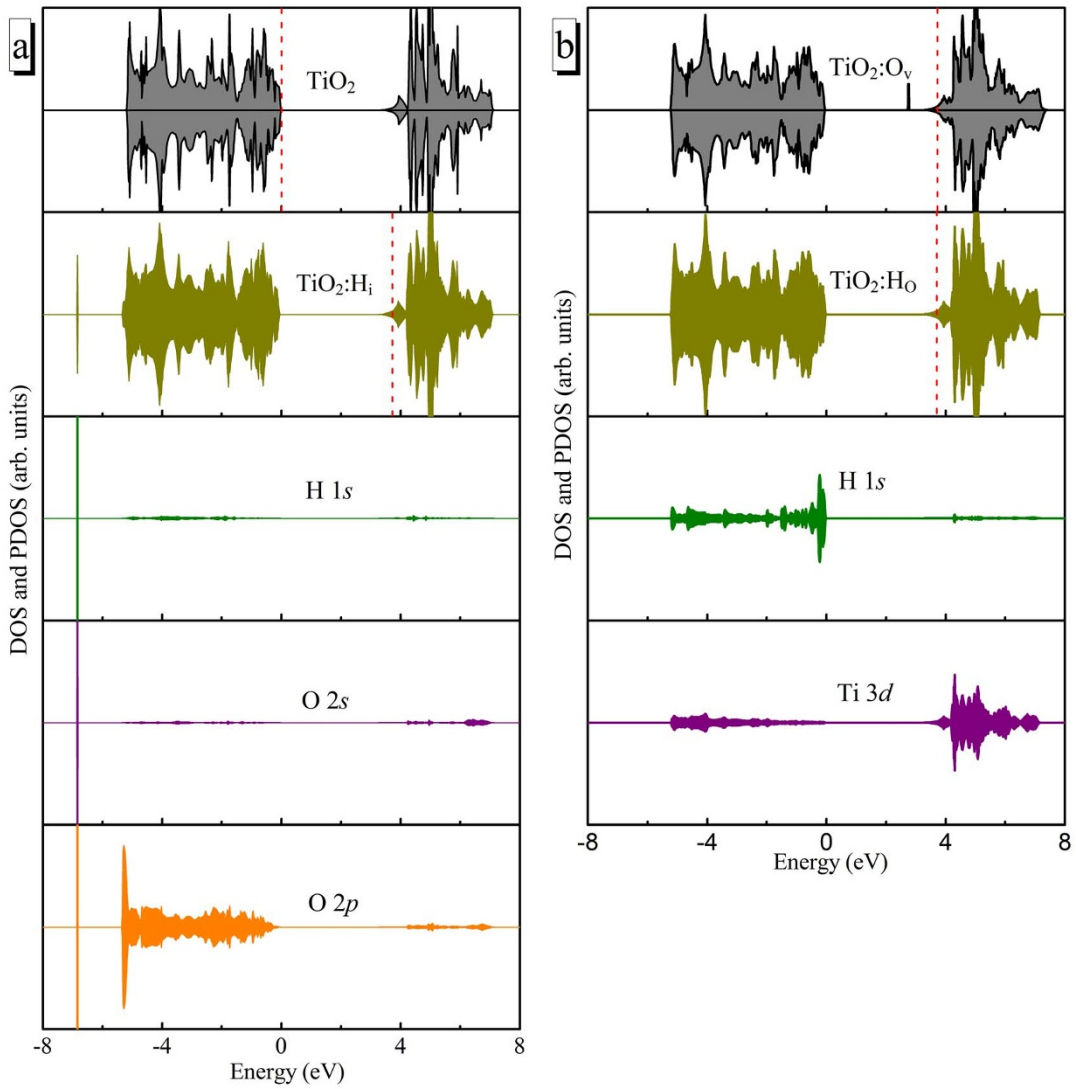

Figure 3 | Total density of states (DOS) and projected density of states (PDOS) of hydrogen doped TiO_2. (a) From top to bottom: total DOS of the perfect crystal; total DOS of the crystal containing H_i; PDOS on the H 1 *s*; and PDOS on 2 *s* and 2 *p* states of the oxygen to which the hydrogen bonds. (b) From top to bottom: total DOS of the crystal containing O_V; total DOS of the crystal containing H_O; PDOS on the H 1 *s*; and PDOS on the nearest-neighbor Ti 3 *d* in TiO_2. As the PDOS on all three adjacent Ti atoms are almost the same, only one of them is shown. The zero energy is at VBM and the vertical dashed lines denote the Fermi levels.

To achieve effective n-type doping, thus getting high concentration of free carriers in the doped semiconductor at thermodynamic equilibrium as that of metal, the donor level $\Delta(+1/0)$ of the dopant, which is defined as the Fermi level position where the formation energies of charge states +1 and 0 are equal[33], must be close to or resonant with the conduction band. Satisfyingly, as shown in Figure 2, the donor levels of both H_i and H_O are in resonance with the conduction band, suggesting that the electron can be effectively injected into the conduction band, thus contributing to n-type conductivity. Therefore, the high solubility of H dopant, together with the shallow donor level, can promise a large carrier concentration, and this results can be used to account for the large n-type conductivity and carrier concentration ($7.8 \times 10^{20}/cm^3$) of TiO_2 film after hydrogen plasma treatment observed experimentally[25].

Electronic structures. In order to reveal the origin of the high solubility and shallow donor levels of H_i and H_O, a closer look at the electronic structures of the doped system is helpful. Figure 3a shows the density of states (DOS) of perfect and H_i doped TiO_2, as well as the projected density of states (PDOS) on hydrogen and oxygen to which the hydrogen bonds. Clearly, there are no defect levels in the bandgap and a sharp peak located at 6.8 eV below the valance band maximum appears upon H_i doping. The PDOS shows that the peak is a hybridization of H 1 *s*, O 2 *s*, and O 2 *p* states, and the other superposition states of these three orbitals are located in the conduction band. This picture is consistent with the bonding and antibonding character of the orbitals, which can be understood from the molecular orbital theory, as pictorially presented in Figure 4a: to bond with hydrogen 1 *s* orbital, the 2 *s* and 2 *p* orbitals of the oxygen must form a symmetric (a_1) combination premised on principles of orbital symmetry matching[37], moreover, since the oxygen 2 *s* and 2 *p* orbitals are fully occupied, one of the three electrons has to occupy the antibonding orbital which is located in the conduction bond without introducing gap states, thus resulting in a shallow donor level in resonance with the conduction band, as indicated in the preceding part. In addition, the strong bonding between hydrogen and oxygen, as implied by the lower lying bonding states, ensures the small formation energy of H_i and hence large solubility. Furthermore, the electronic charge density distribution of the fully symmetric bonding states between hydrogen and oxygen clearly reveals a

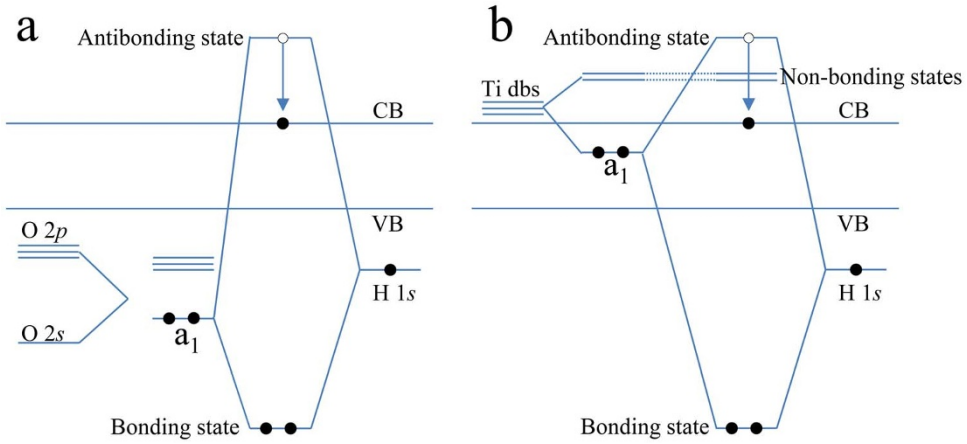

Figure 4 | Details of orbital interaction between H and the adjacent host atoms. (a) The interaction between H 1 *s* orbital and the 2 *s* and 2 *p* orbitals of the oxygen to which the hydrogen bonds in H_i doped TiO_2. (b) The interaction between H 1 *s* orbital and the dangling bonds (dbs) of three adjacent Ti atoms in H_O doped TiO_2. In both cases, the H 1 *s* orbital combines with the fully occupied symmetry-adapted a_1 state, resulting in a bonding state in the valence band (VB) and an antibonding state in the conduction band (CB). The electron that would occupy the antibonding state is then transferred to the conduction band minimum, making both H_i and H_O shallow donors.

strong polar O-H σ bonding orbital (Figure 5a), which is consistent with the analysis based on molecular orbital theory. Finally, we note that the shallow donor nature of H_i in anatase TiO_2 is also consistent with the prediction of the model of hydrogen universal alignment proposed in Ref. 33 and 38.

For Ho, the occupation of hydrogen atom in the oxygen vacancy site effectively eliminates the gap states introduced by O_v and makes the donor level lie in the conduction band, as shown in Figure 3b, thus contributing more free carriers. This phenomenon can be easily understood due to the formation of hydrogen multicenter bonds with the adjacent three Ti atoms: The PDOS on H and the nearest-neighbor Ti atoms exhibit strong hybridization, which is the indication of strong bonding between H and Ti atoms; Moreover, the PDOS on all three adjacent Ti atoms are almost the same due to the combination of the three Ti 3 *d* dangling bonds to form a symmetric (a_1) orbital, and the detailed process of orbital interaction is pictorially illustrated in Figure 4b. Further analysis of electronic charge density distribution of the hydrogen multicenter bonds also reveals that the hydrogen bonds almost equally to the three adjacent Ti atoms (Figure 5b). Therefore, the bonding of H with adjacent Ti atoms makes the antibonding state, which is also the donor level, lie in the conduction band. In addition, since the gap states generally promote the recombination of photogenerated carriers, the removal of these states by hydrogen doping can result in low recombination rate of electrons and holes as revealed by the photoluminescence (PL) emission spectra measurement[25]. Moreover, since hydrogen doping can effectively eliminate the Ti^{3+} ions, the electron paramagnetic resonance (EPR) signal of Ti^{3+} will also disappear after hydrogen doping, as observed in Ref. 25.

Finally, the charge density distribution of the donated electrons by H_i and H_O (Figure 6) shows that the doped electrons by both H_O and H_i are well delocalized among the Ti atoms, indicating effective n-type doping, which is also consistent with the absence of Ti^{3+} spins revealed by the EPR measurement[25]. In addition, the itinerant nature of the doped electron also accounts for the experimentally observed high conductivity. The significant local lattice distortion induced by H_i doping, as shown in Figure 1b, rationalize the formed amorphous disordered shell of TiO_2 nanocrystals after hydrogen plasma process, as this process can introduce large amount of H_i into the TiO_2 lattice. Although large researches indicate that one free electron is often trapped in Ti atoms forming a polaron[39,40], thus limiting the conductivity of electron, we note that when large number of electrons populate in the conduction band, the competition of adjacent polarons through their induced structural distortion may free the trapped electrons, which is also verified by the large electron carrier concentration observed experimentally[25].

LSPR properties of heavily doped semiconductor. The results above indicate that hydrogen is an effective n-type dopant, which can introduce large carrier concentration in the order of magnitude of $10^{21}/cm^3$ or even larger. Then what exactly is the carrier concentration that can realize metal-like optical property-LSPR in TiO_2? Here, we note that the LSPR requires the real part of the complex

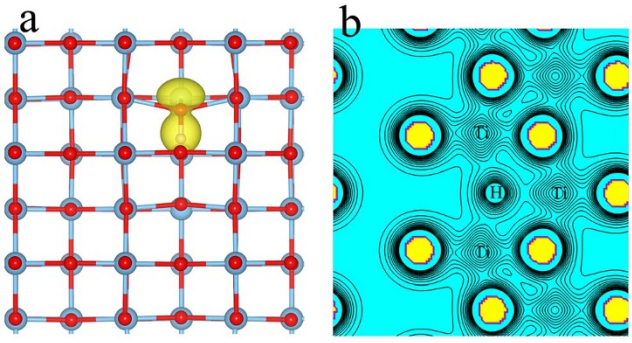

Figure 5 | Electronic charge density distribution of the bonding states between hydrogen and host atoms. (a) Three-dimensional visualization for H_i doped TiO_2, the isosurface is at 0.015 electrons $Å^{-3}$. (b) Two-dimensional contour plot for H_O doped TiO_2 and the contour plot is on the plane containing hydrogen and the adjacent three Ti atoms.

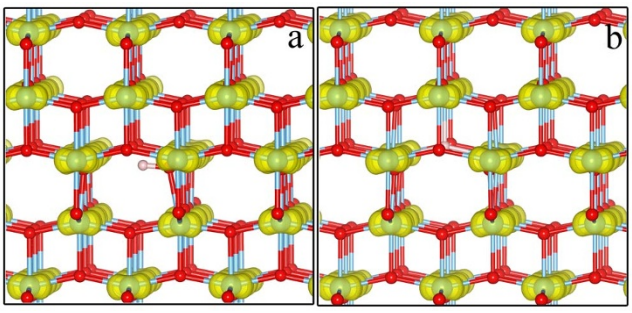

Figure 6 | The charge density distribution of the donated electrons by: (a) H_i. (b) H_O. The atom notations are the same as that in Figure 1.

Table 1 | The parameters used for our calculations of the critical carrier concentration required to make the real part of the permittivity of semiconductor negative at 1000 nm along with the calculated results

Sample	Background permittivity ε_b	Carrier mobility μ [$cm^2V^{-1}s^{-1}$]	Effective mass m^* in unit of free electron mass	Critical carrier concentration [$\times 10^{21}/cm^3$]
TiO_2	6[57]	20[58]	1[45]	6.72
ZnO	3.8[22]	52.6*	0.38[22]	1.62

*The carrier mobility is obtained assuming similar relaxation rate as that of TiO_2, satisfactorily, this value is similar to that of heavily Al doped ZnO.

permittivity to be a negative value ($\varepsilon' < 0$ for $\omega < \omega_C$), thus it puts a lower limit on the carrier concentration. To get the permittivity of heavily doped semiconductor, we turn to the Drude model[29,30] which describes the free electron response to electromagnetic wave as equation (4):

$$\varepsilon(\omega) = \varepsilon' + i\varepsilon'' = \varepsilon_b - \frac{\omega_p^2}{(\omega^2+\gamma^2)} + i\frac{\omega_p^2\gamma}{(\omega^2+\gamma^2)\omega} \quad (4)$$

Where ε_b is the background permittivity which describes the polarization response of the core electrons; ω_p is the plasma frequency; and γ is the Drude relaxation rate which is responsible for the scattering and Ohmic losses. Based on the formula, the critical concentration to achieve metal-like properties ($\varepsilon' < 0$ for $\omega < \omega_C$, here ω_C is chosen to be corresponding to the wavelength of 1000 nm which is relevant to photocatalysis. From the following equation (5), shorter wavelength will require larger carrier concentration) is given by the following equation (5):

$$n > \frac{\varepsilon_0 m^*}{e^2}\varepsilon_b(\omega_c^2+\gamma^2) \quad (5)$$

Where ε_0 is the vacuum permittivity, e is the electron charge, m^* is the carrier effective mass, and γ is approximated to be $\gamma = e/\mu m^*$ in which μ is the carrier mobility[22]. For our specific sample TiO_2, the parameters used for our calculations and results are listed in Table 1.

Surprisingly, the carrier concentration introduced by hydrogen doping can exceed the required critical concentration producing LSPR. Therefore, we further estimate the LSPR effect of TiO_2 with this critical carrier concentration. The model of a 2 nm thick spherical shell with a diameter of 20 nm, which is comparable with the experimental samples[25], is used in our further calculations. The LSPR absorption spectra and the enhanced electric field are shown in Figure 7. The results show that the LSPR wavelength is in the infrared region of the electromagnetic spectra due to the smaller carrier concentration compared with that of metal, which can supplement the absorption of classic noble metal NPs whose absorption is generally in the visible light range[41,42]. In addition, the infrared LSPR of heavily doped TiO_2 can also be readily used in infrared bioimaging and spectroscopy[43,44], where extending the LSPR of noble metal NPs further into the infrared region is quite challenging.

On the other hand, the enhanced electric field contour also indicates that the near field enhancement of the LSPR effect of the heavily doped semiconductor is comparable with that of noble metal NPs[13,42]. Similar to the LSPR of noble metal NPs, the LSPR wavelength can also be easily tuned by particle sizes, dimensions, and local dielectric environment, to cover a wide range of wavelengths.

According to the above LSPR properties of doped semiconductor, some reasonable LSPR phenomena can be inferred: as the LSPR wavelength is located in the infrared region, the doped semiconductors will show remarkable absorption in this region (Figure 7) in photocatalytic reactions. As another significant effect of LSPR, the near-field enhancement (Figure 7) will not only increase the light absorption rate but also decrease the recombination of photogenerated carriers[15], thus significantly improving the overall photocatalytic performance of the systems.

Discussion

For the specific carrier concentration of the samples ($2.27 \times 10^{20}/cm^3$) reported by Wang et al[25], the corresponding wavelength for the real part of permittivity to be negative is estimated to be 5617 nm, then the absorption within 2000 nm as reported in the experiment may be mainly due to the intraband transition of the large amount of free carries rather than LSPR, it is noted that broad absorption peak ranging from visible region to infrared region due to intraband transition of free carriers has also been observed in heavily Nb-doped TiO_2[45]. However, when the interband transition is induced by the ultraviolet light, large number of additional photogenerated electrons will be populated in the surface shell, then it may induce LSPR effect near or within 2000 nm. In addition, the photogenerated electrons are recently reported to induce LSPR in ZnO nanocrystals[46].

In the present work, according to the Drude model, we have estimated the critical concentration of carriers ($6.72 \times 10^{21}/cm^3$) [Table 1] for TiO_2 to show LSPR in the near infrared region in which some kinds of photocatalytic reactions can be driven, this critical concentration is found to be significantly higher than that ($2.27 \times 10^{20}/cm^3$) obtained in the previous work with citation of Ref. 25. Therefore, we conclude that the absorption within 2000 nm as reported in the experiment should be mainly due to the intraband transition of the large amount of free carries rather than LSPR. In addition, based on the first-principles calculations, it is inferred theoretically that the critical concentration of carriers can actually been obtained by proper hydrogen plasma doping. Thus future work should be devoted to realizing this promising H-doped TiO_2 plasmonic photocatalyst.

By the way, because the absorption spectra in the near infrared region of Ref. 25 originate mainly from the intraband transition of

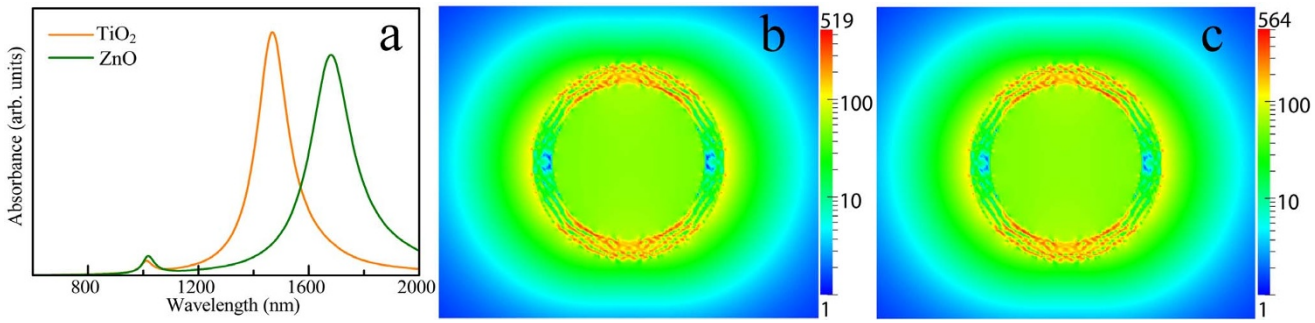

Figure 7 | The LSPR properties of TiO_2 and ZnO. (a) The LSPR absorption spectra of TiO_2 and ZnO with the critical carrier concentration as listed in Table 1. (b) and (c) are the corresponding LSPR enhanced electric field contours ($|E|^2/|E_0|^2$) of TiO_2 and ZnO at the LSPR wavelengths, respectively, where E is the LSPR enhanced electric field, and E_0 is the electric field of incident electromagnetic wave.

carriers rather than the localized surface plasmon resonance (LSPR) absorption of carriers, the LSPR absorption presented in the present work is different from the absorption spectra in Ref. 25. Furthermore, it is exclusively because the doping level of hydrogen in their $TiO_{2-x}H_x$ sample is not high enough that the LSPR within 2000 nm cannot be induced, whereas the qualitative trends of PL spectra and EPR data should be identical in the present work and Ref. 25.

Additionally, large amount of experimental and theoretical results indicate that hydrogen also has a large solubility and the donor level of H_i and H_O are also resonant with the conduction band in ZnO, another important photocatalyst[33,37,47,48], thus high carrier concentration should be expected by hydrogen doping in ZnO, too. Moreover, because of the smaller electron effective mass and background permittivity of ZnO compared with TiO_2, the critical carrier concentration for it to exhibit metal-like optical properties at wavelength of 1000 nm is estimated to be only $1.616 \times 10^{21}/cm^3$ assuming similar relaxation rate as that of TiO_2, indicating that it may be easier to realize LSPR in ZnO by hydrogen doping. The LSPR absorption spectra and enhanced electric field, as shown in Figure 7, demonstrate similar LSPR properties as that of TiO_2, thus also beneficial for photocatalysis.

In summary, we reveal that the strong bonding of hydrogen with the host atoms can ensure large solubility and shallow donor levels of H_i and H_O, consequently, introducing carrier concentration large enough to realize LSPR properties in semiconductor photocatalyst TiO_2 at wavelengths relevant to photocatalysis. Moreover, the infrared LSPR absorption can supplement that of noble metal whose absorption is generally in the visible region, thus making it possible to extend the light response of photocatalyst to infrared region. The near field enhancement property is shown to be comparable with that of noble metal NPs. In addition, it is expected that similar LSPR properties can be realized in ZnO by hydrogen doping. Finally, we expect these entirely new discoveries not only to be a key guideline for the creation of highly efficient noble-metal-free plasmonic photocatalyst systems but also to have a much wider impact in potentially any applications where infrared LSPR is essential, such as infrared bioimaging and spectroscopy.

Methods

The total energies and electronic structures are obtained based on the spin-polarized density functional theory (DFT) calculations using the projector augmented wave (PAW) pseudopotentials as implemented in the Vienna *ab initio* Simulation Package (VASP) code[49,50]. Heyd–Scuseria–Ernzerhof (HSE06) hybrid functional, which can provide good physical descriptions of defects in wide-bandgap semiconductors[51–53], is used in our calculations. A $3 \times 3 \times 1$ supercell with the lattice parameters [a = 3.776 Å, c/a = 2.512 Å] is used to simulate the bulk TiO_2 and a hydrogen atom is introduced into the lattice to simulate the corresponding H_i or H_O doped TiO_2. The electron wave function is expanded in plane waves up to a cutoff energy of 400 eV to provide sufficient precision. The Brillouin zone is sampled with $2 \times 2 \times 2$ Γ-centered k-points[54]. The atomic positions of all atoms are fully relaxed until the residual force is smaller than 0.02 eV/Å. The total and projected densities of states (TDOS and PDOS) are calculated at the equilibrium volume using the tetrahedron method with Blöchl corrections for accuracy[55].

The LSPR absorption spectra and enhanced electric field distribution are obtained by solving the Maxwell's equations numerically based on the discrete dipole approximation (DDA) as implemented in the DDSCAT code[31,32,56]. The DDA approximates the object of interest by an array of polarizable points, and there is no restriction as to which of the array sites is occupied, which means that DDA can represent an object or multiple objects of arbitrary shape and composition. Thus it is very useful for the present study. The permittivity of TiO_2 is obtained based on the Drude model as detailed in the Results part. All DDA calculations refer to vacuum as the external dielectric medium. For full convergence of the calculations, an inter-dipole distance of 0.2 nm is used.

1. Yang, K., Dai, Y., Huang, B. & Whangbo, M.-H. Density functional characterization of the band edges, the band gap states, and the preferred doping sites of halogen-doped TiO_2. *Chem. Mater.* **20**, 6528–6534 (2008).
2. Yang, K., Dai, Y. & Huang, B. Origin of the photoactivity in boron-doped anatase and rutile TiO_2 calculated from first principles. *Phys. Rev. B* **76**, 195201–195201 (2007).
3. Asahi, R., Morikawa, T., Ohwaki, T., Aoki, K. & Taga, Y. Visible-light photocatalysis in nitrogen-doped titanium oxides. *Science* **293**, 269–271 (2001).
4. Zheng, L. *et al.* Network Structured SnO_2/ZnO Heterojunction Nanocatalyst with High Photocatalytic Activity. *Inorg. Chem.* **48**, 1819–1825 (2009).
5. Etgar, L. *et al.* High Efficiency Quantum Dot Heterojunction Solar Cell Using Anatase (001) TiO_2 Nanosheets. *Adv. Mater.* **24**, 2202–2206 (2012).
6. Yang, M.-Q. & Xu, Y.-J. Selective photoredox using graphene-based composite photocatalysts. *Phys. Chem. Chem. Phys.* **15**, 19102–19118 (2013).
7. Zhang, N., Zhang, Y. & Xu, Y.-J. Recent progress on graphene-based photocatalysts: current status and future perspectives. *Nanoscale* **4**, 5792–5813 (2012).
8. Zong, X. *et al.* Enhancement of photocatalytic H_2 evolution on CdS by loading MoS_2 as cocatalyst under visible light irradiation. *J. Am. Chem. Soc.* **130**, 7176–7177 (2008).
9. Li, R. *et al.* Spatial separation of photogenerated electrons and holes among {010} and {110} crystal facets of $BiVO_4$. *Nat. Commun.* **4**, 1432–1432 (2013).
10. Nakata, K. & Fujishima, A. TiO_2 photocatalysis: design and applications. *J. Photochem. Photobiol. C* **13**, 169–189 (2012).
11. Chen, X., Liu, L., Yu, P. Y. & Mao, S. S. Increasing solar absorption for photocatalysis with lack hydrogenated titanium dioxide nanocrystals. *Science* **331**, 746–750 (2011).
12. Hoffmann, M. R., Martin, S. T., Choi, W. & Bahnemann, D. W. Environmental applications of semiconductor photocatalysis. *Chem. Rev.* **95**, 69–96 (1995).
13. Zhang, X., Chen, Y. L., Liu, R.-S. & Tsai, D. P. Plasmonic photocatalysis. *Rep. Prog. Phys.* **76**, 046401–046401 (2013).
14. Wang, P., Huang, B., Dai, Y. & Whangbo, M.-H. Plasmonic photocatalysts: harvesting visible light with noble metal nanoparticles. *Phys. Chem. Chem. Phys.* **14**, 9813–9825 (2012).
15. Liu, Z., Hou, W., Pavaskar, P., Aykol, M. & Cronin, S. B. Plasmon resonant enhancement of photocatalytic water splitting under visible illumination. *Nano Lett.* **11**, 1111–1116 (2011).
16. Liu, L., Ouyang, S. & Ye, J. Gold-nanorod-photosensitized titanium dioxide with wide-range visible-light harvesting based on localized surface plasmon resonance. *Angew. Chem. Int. Ed.* **52**, 6689–6693 (2013).
17. Awazu, K. *et al.* A plasmonic photocatalyst consisting of silver nanoparticles embedded in titanium dioxide. *J. Am. Chem. Soc.* **130**, 1676–1680 (2008).
18. Wang, P. *et al.* Highly efficient visible-light plasmonic photocatalyst Ag@AgBr. *Chem. Eur. J.* **15**, 1821–1824 (2009).
19. Wang, P. *et al.* Highly efficient visible light plasmonic photocatalysts Ag@Ag(Cl,Br) and Ag@AgCl-AgI. *ChemCatChem* **3**, 360–364 (2011).
20. Wang, P. *et al.* Ag@AgCl: A highly efficient and stable photocatalyst active under visible light. *Angew. Chem. Int. Ed.* **47**, 7931–7933 (2008).
21. Ma, X., Dai, Y., Guo, M., Zhu, Y. & Huang, B. Insights into the adsorption and energy transfer of Ag clusters on the AgCl (100) surface. *Phys. Chem. Chem. Phys.* **15**, 8722–8731 (2013).
22. Naik, G. V., Shalaev, V. M. & Boltasseva, A. Alternative plasmonic materials: Beyond gold and silver. *Adv. Mater.* **25**, 3264–3294 (2013).
23. Tian, J. *et al.* A Bi_2WO_6-based hybrid photocatalyst with broad spectrum photocatalytic properties under uv, visible, and near-infrared irradiation. *Adv. Mater.* **25**, 5075–5080 (2013).
24. Wang, G. *et al.* $Cu_2(OH)PO_4$, a near-infrared-activated photocatalyst. *Angew. Chem. Int. Ed.* **52**, 4810–4813 (2013).
25. Wang, Z. *et al.* H-doped black titania with very high solar absorption and excellent photocatalysis enhanced by localized surface plasmon resonance. *Adv. Funct. Mater.* **23**, 5444–5450 (2013).
26. Panayotov, D. A. & Yates Jr, J. T. N-Type doping of TiO_2 with atomic hydrogen-observation of the production of conduction band electrons by infrared spectroscopy. *Chem. Phys. Lett.* **436**, 204–208 (2007).
27. Lu, J., Dai, Y., Jin, H. & Huang, B. Effective increasing of optical absorption and energy conversion efficiency of anatase TiO_2 nanocrystals by hydrogenation. *Phys. Chem. Chem. Phys.* **13**, 18063–18068 (2011).
28. Liu, L., Yu, P. Y., Chen, X., Mao, S. S. & Shen, D. Z. Hydrogenation and disorder in engineered black TiO_2. *Phys. Rev. Lett.* **111**, 065505–065505 (2013).
29. Drude, P. Zur Elektronentheorie der Metalle. *Ann. Phys.* **306**, 566–613 (1900).
30. Ashcroft, N. W. & Mermin, N. D. [The Drude Theory of Metals] *Solid State Physics* [16–19] (Thomson Learning, 1976).
31. Purcell, E. M. & Pennypacker, C. R. Scattering and absorption of light by nonspherical dielectric grains. *ApJ* **186**, 705–714 (1973).
32. Draine, B. T. The discrete-dipole approximation and its application to interstellar graphite grains. *ApJ* **333**, 848–872 (1988).
33. Van de Walle, C. G. & Neugebauer, J. Universal alignment of hydrogen levels in semiconductors, insulators and solutions. *Nature* **423**, 626–628 (2003).
34. Finazzi, E., Valentin, C. D., Pacchioni, G. & Selloni, A. Excess electron states in reduced bulk anatase TiO_2: Comparison of standard GGA, GGA + U, and hybrid DFT calculations. *J. Chem. Phys.* **129**, 154113–154113 (2008).
35. Islam, M. M., Calatayud, M. & Pacchioni, G. Hydrogen adsorption and diffusion on the anatase TiO_2 (101) surface: A first-principles investigation. *J. Phys. Chem. C* **115**, 6809–6814 (2011).
36. Raghunath, P., Huang, W. F. & Lin, M. C. Quantum chemical elucidation of the mechanism for hydrogenation of TiO_2 anatase crystals. *J. Chem. Phys.* **138**, 154705–154705 (2013).

37. Janotti, A. & Van de Walle, C. G. Hydrogen multicentre bonds. *Nat. Mater.* **6**, 44–47 (2007).
38. Kilic, C. & Zunger, A. n-type doping of oxides by hydrogen. *Appl. Phys. Lett.* **81**, 73–75 (2002).
39. Di Valentin, C. & Selloni, A. Bulk and surface polarons in photoexcited anatase TiO_2. *J. Phys. Chem. Lett.* **2**, 2223–2228 (2011).
40. Deskins, N. A. & Dupuis, M. Electron transport via polaron hopping in bulk TiO_2: A density functional theory characterization. *Phys. Rev. B* **75**, 195212–195212 (2007).
41. Aroca, R. F. Plasmon enhanced spectroscopy. *Phys. Chem. Chem. Phys.* **15**, 5355–5363 (2013).
42. Linic, S., Christopher, P. & Ingram, D. B. Plasmonic-metal nanostructures for efficient conversion of solar to chemical energy. *Nat. Mater.* **10**, 911–921 (2011).
43. Liu, X. *et al*. Au–Cu_{2-x}Se heterodimer nanoparticles with broad localized surface plasmon resonance as contrast agents for deep tissue imaging. *Nano Lett.* **13**, 4333–4339 (2013).
44. Law, S., Yu, L., Rosenberg, A. & Wasserman, D. All-semiconductor plasmonic nanoantennas for infrared sensing. *Nano Lett.* **13**, 4569–4574 (2013).
45. Kurita, D., Ohta, S., Sugiura, K., Ohta, H. & Koumoto, K. Carrier generation and transport properties of heavily Nb-doped anatase TiO_2 epitaxial films at high temperatures. *J. Appl. Phys.* **100**, 096105–096105 (2006).
46. Faucheaux, J. A. & Jain, P. K. Plasmons in photocharged ZnO nanocrystals revealing the nature of charge dynamics. *J. Phys. Chem. Lett.* **4**, 3024–3030 (2013).
47. Hofmann, D. M. *et al*. Hydrogen: A relevant shallow donor in zinc oxide. *Phys. Rev. Lett.* **88**, 045504–045504 (2002).
48. Cox, S. F. J. *et al*. Experimental confirmation of the predicted shallow donor hydrogen state in zinc oxide. *Phys. Rev. Lett.* **86**, 2601–2604 (2001).
49. Kresse, G. & Hafner, J. Ab initio molecular dynamics for liquid metals. *Phys. Rev. B* **47**, 558–561 (1993).
50. Kresse, G. & Furthmüller, J. Efficient iterative schemes for ab initio total-energy calculations using a plane-wave basis set. *Phys. Rev. B* **54**, 11169–11186 (1996).
51. Heyd, J., Scuseria, G. E. & Ernzerhof, M. Erratum: "Hybrid functionals based on a screened Coulomb potential" [J. Chem. Phys. 118, 8207 (2003)]. *J. Chem. Phys.* **124**, 219906–219906 (2006).
52. Heyd, J., Scuseria, G. E. & Ernzerhof, M. Hybrid functionals based on a screened Coulomb potential. *J. Chem. Phys.* **118**, 8207–8215 (2003).
53. Choi, M., Oba, F., Kumagai, Y. & Tanaka, I. Anti-ferrodistortive-like oxygen-octahedron rotation induced by the oxygen vacancy in cubic $SrTiO_3$. *Adv. Mater.* **25**, 86–90 (2013).
54. Monkhorst, H. J. & Pack, J. D. Special points for Brillouin-zone integrations. *Phys. Rev. B* **13**, 5188–5192 (1976).
55. Blöchl, P. E., Jepsen, O. & Andersen, O. K. Improved tetrahedron method for Brillouin-zone integrations. *Phys. Rev. B* **49**, 16223–16233 (1994).
56. Flatau, P. J. & Draine, B. T. Discrete-dipole approximation for scattering calculations. *J. Opt. Soc. Am. A* **11**, 1491–1491 (1994).
57. Jellison, G. E., Boatner, L. A., Budai, J. D., Jeong, B. S. & Norton, D. P. Spectroscopic ellipsometry of thin film and bulk anatase (TiO_2). *J. Appl. Phys.* **93**, 9537–9541 (2003).
58. Jeong, B. S., Norton, D. P. & Budai, J. D. Conductivity in transparent anatase TiO_2 films epitaxially grown by reactive sputtering deposition. *Solid State Electron* **47**, 2275–2278 (2003).

Acknowledgments

This work is supported by the National Basic Research Program of China (973 program, 2013CB632401), National Science foundation of China under Grant 11374190 and 21333006, and the Natural Science Foundation of Shandong Province under Grant number ZR2011AM009, ZR2013AM021, and 111 Project B13029. We also thank the National Supercomputer Center in Jinan for providing high performance computation.

Author contributions

Y.D. and B.B.H. designed the research. X.C.M. and L.Y. performed the density functional theory and DDSCAT calculations. X.C.M. and Y.D. prepared the manuscript. All authors contributed to the scientific discussions.

Additional information

Competing financial interests: The authors declare no competing financial interests.

How to cite this article: Ma, X.C., Dai, Y., Yu, L. & Huang, B.B. Noble-metal-free plasmonic photocatalyst: hydrogen doped semiconductors. *Sci. Rep.* **4**, 3986; DOI:10.1038/srep03986 (2014).